



1 Article

The Actuation Mechanism of 3D Printed Flexure-

3 Based Robotic Microtweezers

- 4 Alexander Almeida¹, George Andrews¹, Devina Jaiswal^{1,2}, and Kazunori Hoshino¹
- Department of Biomedical Engineering University of Connecticut, 260 Glenbrook Rd, Storrs, Connecticut
 06269, USA
- Department of Biomedical Engineering, Western New England University, 1215 Wilbraham Rd,
 Springfield, Massachusetts 01119, USA
- 9 Received: date; Accepted: date; Published: date

Abstract: We report on the design and modeling of a 3D printed flexure-based actuation mechanism for robotic microtweezers, the main body of which is a single piece of nylon. Our design aims to fill a void in sample manipulation between two classes of widely used instruments: nano-scale and macro-scale robotic manipulators. The key component is a uniquely designed cam flexure system, which linearly translates the bending of a piezoelectric bimorph actuator into angular displacement. 3D printing made it possible to realize the fabrication of the cam with a specifically calculated curve, which would otherwise be costly using conventional milling techniques. We first characterize 3D printed nylon by studying sets of simple cantilevers, which provided fundamental characteristics that can be used for further designs. The finite element method analysis based on the obtained material data matched well with the experimental data. The tweezers showed angular displacement from 0° to 10° linearly to the deflection of the piezo actuator (0-1.74 mm) with the linearity error of 0.1° . Resonant frequency of the system with/without working tweezer tips was discovered as 101 Hz and 127 Hz, respectively. Our design provides simple and low-cost construction of a versatile manipulator system for samples in the micro/meso-scale (0.1-1 mm).

Keywords: manipulator; flexure; 3D-printing; micro/meso-scale manipulation; piezo bimorph actuator

1. Introduction

We propose the use of commercially available 3D printing-based fabrication to create an actuation mechanism that fills the void in sample manipulation between two classes of widely used bioinstruments, nano-scale instruments and macro-scale instruments. Specifically, we target manipulation in size range 100 μm to 1 mm, which we refer to as micro/meso-scale. Common techniques of nanoscale manipulation include: Atomic Force Microscopy (AFM)-based nanomanipulation systems (target sample range between 200 nm - 10 μm) [1-3] and MEMS microgrippers (typical operational range < 100 μm) [4-6], which rely on the use of lithography-based micromachined cantilevers or manipulators. On the macro scale, robotic systems, such as the Da Vinci Surgical System [7] which targets samples at least 1 mm or larger [8], are built-through conventional precision machining [9-10]. In this paper, we will demonstrate that the technology of 3D printing is a suitable method to fabricate the mechanical manipulator that occupies the promising area that lies between micromachining and precision machining.

There have been studies of micromanipulators targeting micro/meso-scale samples. Arai et al. demonstrated the capability of a finger-like piezo-electric actuated hybrid micromanipulator for 3D manipulation of microscopic objects by picking up and moving a micro-ball of <10 μ m [11]. This design featured baseplates and a number of joints with two chopstick-like glass needles at the end, making it complex to assemble and suffering initial issues with tip alignment. Tabachkova et al.

46 47

48 49

50

51 52

53

54

55

56 57

58

59

60

61

62

63

64

65 66

67

68

69

70

72

73

74

75

76

77

78

79 80

81 82

83

84

85

86 87

88

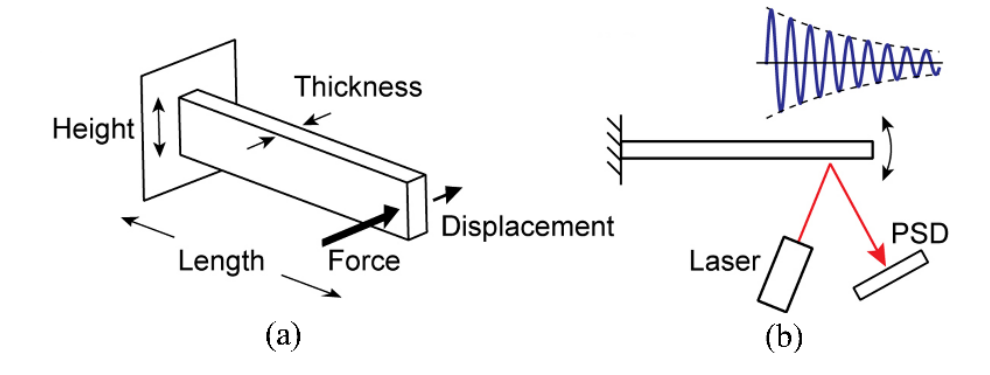
demonstrated the value of shape-memory alloys (SMAs) as an actuator for a micromanipulator. They demonstrated that a 5-14 µm thick TiNiCu alloy ribbon along with an elastic alloy could be used as an actuator in a microtweezer design to manipulate graphene sheets [12]. In this experiment, the micromanipulator exhibited an operational range between 0 nm - 1200 nm under the influence of an external source of thermal energy [12]. The major disadvantage of SMAs is the difficulty in controlling displacement because of thermomechanical nonlinearity [13]. Reuben et al. demonstrated the capability of micromanipulation using a pneumatic actuator by manipulating 200 µm zirconium micro-beads. The team proved the potential of pneumatic actuation to produce some of the highest force and power densities of actuation options at the microscale, including a maximum tip opening amplitude of 1 mm and a maximum force output of 50 mN [14]. Pneumatic actuation requires integration of pumps, valves and tubing, which tend to make the system larger. Here we report design, fabrication, and testing of a 3D printed flexure-based actuation mechanism using a piezo bimorph actuator. The mechanism is intended for microtweezers targeted for micro/meso-scale (100 µm to 1 mm) samples. The body of our design is a single 3D printed piece of nylon. The use of 3D printing for flexure-based actuation is a new concept we proposed in our recent study, which not only reduces material costs and scrap by omitting extensive machining, but allows for the design of application-oriented, versatile actuation mechanisms. We have proven that the flexure works for a nanopositioning stage previously in [15], using 3D printing of Titanium. In a related study, Wei et al. reported on a fabrication and testing of a flexure parallel Mechanism made of stainless steel 316L [16]. Here we use polymer to ensure that the piece would be cheap and disposable, which is important for biomedical applications. The use of a piezo bimorph actuator is advantageous because it generates a relatively large deflection (~sub millimeter range), which fits our target range. 3D printing allows for the easy production of a part that matches specific design requirements. In this case, 3D printing makes it possible to make the cam with a very specific, calculated curve, that linearly transforms the deflection of the actuator to the angular displacement of the flexure. The necessary level of precision of cam specifications would be costly with alternative fabrication methods, such as milling or drilling.

71 2. Materials and Methods

2.1 The material for 3D printing

We used 3D printed nylon (PA2200, EOS GmbH, Münich, Germany), provided by Shapeways (New York, NY). We evaluated the characteristics of the materials through fundamental cantilever testing. The specified parameters including Young's modulus (E) and density (ρ) can be used to further model the actuation mechanism, specifically the flexure that supports the moving arm of the microtweezers.

To test the material properties of the nylon, 3 pieces of 6 different designs (designs #1-#6) were printed totaling to 18 cantilevers. We used design length of 30 mm (#1,2,3) and 40 mm (#4,5,6), and design thickness of 0.8 mm (#1 and #4), 1.0 mm (#2 and #5), and 1.2 mm (#3 and #6). The design height was 5 mm for all the cantilevers. Using these cantielvers, we determine the spring constant (k) and resonant frequency (f) of each piece. The Young's modulus (E) and density (ρ) of the material were then calculated and compared to the values provided by the material data sheet. Prior to experimental testing, each cantilever was measured for dimensions of length (I), height (I), and thickness (I) using a digitally calibrated caliper and a micrometer (Mitutoyo, Kawasaki, Japan); these dimensions are pictured in Figure 1(a). The dimensions of width and thickness were measured in three locations: close point, midpoint, and farpoint. These three measurements were then averaged. Table 1 summarizes the measured values.



91

92

93

94

95

96

97

98

99

100

101

102

103 104

105

106

107

108

109

110

111

112

113

114

115

116

117

118

119

120

121

Figure 1. 3D printed nylon cantilever diagrams. (a) The defined dimensional variables. (b) System diagram of the experimental setup used for cantilever resonant frequency analysis.

The force-displacement relationship was measured in the following way: We applied the force via a simple stepper motor and force-sensing arm connected to a force sensor in a form of a load cell. The force-sensing arm made contact with the cantilever while movement of the arm was controlled by a serial communication between the stepper motor and MATLAB® through an USB port. The load cell was calibrated by applying 150 incremental steps of 1.60×10^{-4} N of known masses. From this, it was determined that the sensitivity of the probe was $0.786 \text{ V/}\mu\text{N}$. Movement of each nylon cantilever was recorded via 30 snapshots from a microscope for 30 corresponding steps of the stepper motor. The recorded 30 images were processed in MATLAB® using a custom script that tracks specified search areas on a set of TIFF files. The cantilever force and displacement values were then plotted against each other and a least squares regression line was used to determine the force-displacement slope, which represents the spring constant (kd) of the nylon cantilever, which is expressed as:

$$k_{\rm cl} = \frac{Eht_1^3}{4l^3} \tag{1}$$

Using Equation (1), the Young's moduli (E) can be found using the spring constant (kd) in conjunction with the dimensions of length (l), height (h), and thickness (t_1). The resulting Young's moduli E1 from these measurements were more compliant than the expected Young's modulus of nylon P2200 (1700 MPa) by about a factor of two (see Table 2). This phenomenon is due to the effects of surface porosity of the 3D printed nylon cantilevers. The design thicknesses of the cantilevers (0.8 mm – 1.2 mm) were close to the minimum wall thickness (0.7mm) allowed by the company (Shapeways, NY, USA). As the dimensions of a printed part become smaller, the mechanical characteristics are more affected by the surface porosity. This means that the outermost dimensions of the cantilevers, as measured with a digital micrometer, do not accurately represent the bulk material dimensions and thus the bulk material properties, as we discussed for 3D printed titanium cantilevers in [15]. Characteristics of thin-walled porous 3D printed materials have been reported in literature [17-18]. Differences larger than 20% have been reported in [17], and large experimental variations were also observed in [18]. In order to account for the effects of surface porosity, an adjustment of 2δ was applied to the thickness dimension of the cantilevers. By applying different values of δ to consider the inner thickness and replacing t_1 in Equation (1) with $t_2 = t_1 - 2\delta$, we found that the Young's moduli E_2 became closest to the datasheet value of 1700 MPa when $2\delta = 0.23$ mm (see Table 2). This indicates the presence of an additional 115 μ m of non-contributional porous nylon polymer on each side of the cantilever. The maximum percentage difference between the modified Young's moduli and the expected Young's modulus was ~15%, calculated from cantilever design #5.

Table 1. Dimensional Measurements: 3D Printed Nylon Cantilevers

Design	<i>l</i> (mm)	<i>h</i> (mm)	<i>t</i> ₁ (mm)	<i>t</i> ₂ (mm)
#1	30.2	5.11	0.806	0.576
#2	29.9	5.11	0.879	0.649

#3	29.8	5.12	0.944	0.714
#4	40.0	5.14	1.00	0.774
#5	40.2	5.14	1.07	0.840
#6	40.3	5.12	1.13	0.901

Table 2. Static Analysis: 3D Printed Nylon Cantilevers

Design	k (N/m)	E1 (MPa)	E ₂ (MPa)	Expected E (MPa)
#1	15.7	623	1,700	1,700
#2	20.6	637	1,600	1,700
#3	30.4	714	1,650	1,700
#4	39.0	796	1,730	1,700
#5	55.9	961	1,990	1,700
#6	65.6	961	1,910	1,700

The dynamic parameters of the nylon material were also measured. We employed a laser which cast a beam onto a reflective piece of aluminum adhered to a secured cantilever; this setup can be seen in Figure 1(b). The reflected beam from the aluminum was received by a photodiode position detector (Hamamatsu S5990). When the cantilever is bent, the laser reflection is altered, and thus the reflection on the photodiode is altered resulting in a change in current. A thin piece of aluminum foil was mounted onto each of the 18 cantilevers using a sticky wax material. The change in weight due to the aluminum strip and wax material was measured for each cantilever and considered as an additional mass $\Delta m_{\rm cl}$ to the effective mass when considering the resonant frequency:

$$f_{\rm cl} = \frac{1}{2\pi} \sqrt{\frac{k_{\rm cl}}{m_{\rm cl} + \Delta m_{\rm cl}}} \tag{2}$$

Here, m_{cl} is the effective mass of the cantilever approximated as follows:

$$m_{\rm cl} = \frac{33}{140} \cdot \rho t_2 lh \tag{3}$$

Note that $\rho t_2 lh$ in Equation (3) is the actual mass of the cantilever and requires the cantilever dimensional measurements to be found. To be consistent, the inner thickness (t_2) was used to consider the bulk volume in Equation (3). One-by-one the 18 cantilevers were secured onto this experimental setup and given an impulse via a thin metal rod flicked on the free-moving end of the cantilever. The signals from the position detector were recorded with a National Instruments myDAQ device at a sampling frequency of 10 kHz for 2 seconds. The recorded signal of each cantilever was analyzed in MATLAB® using an envelope mapping function with an exponential curve-fitting algorithm to determine the decay time constant (τ), and a single sided amplitude spectrum FFT to determine the signal's resonant frequency (f_{cl}). The equations used for exponential curve fitting and the calculation of the decay time constant (τ) can be seen in Equations (4) and (5), respectively.

$$y(t) = a \cdot e^{-bt} + c \tag{4}$$

$$\tau = \frac{1}{h} \tag{5}$$

In order to find the density (ρ) of the 3D printed nylon material, Equations (2) and (3) were deployed. The resulting densities (ρ = 0.84 ± 0.24 g/cm³) were comparable to the PA 2200 material data sheet's value of 0.93 g/cm³ (see Table 3). These experimentally calculated densities were also compared against the average of three 3D printed cubes each sized at 1 cm³ with an average density of 0.953 g.

Table 3. Resonant Frequency Analysis: 3D Printed Nylon Cantilevers

Design	f(Hz)	τ	ho (g/cm3)
#1	143	2047.8	0.584
#2	193	1909.4	0.586
#3	239	1447.2	1.25
#4	77	4384.2	0.866
#5	90.9	2727.3	0.875
#6	127	2335.2	0.866

2.2 Piezo Basic Characterization

This system requires piezo actuation as system input and transforms this motion into tweezer angular displacement for sample handling. We used a piezoelectric bimorph actuator which sized 40 mm \times 10 mm \times 0.5 mm (Steminc, FL.). The piezoplate is controlled via the output voltage of an 8-bit digital-to-analog converter (DAC) whose voltage ranges between 0 – 5 V. This output voltage is then amplified in the range of -45 V to 45 V using a high voltage operational amplifier (Analog Devices, ADA4700). A characterization of the relationship between the applied voltage to the piezoplate and the corresponding deflection of the piezoplate can be seen in Figure 2(a).

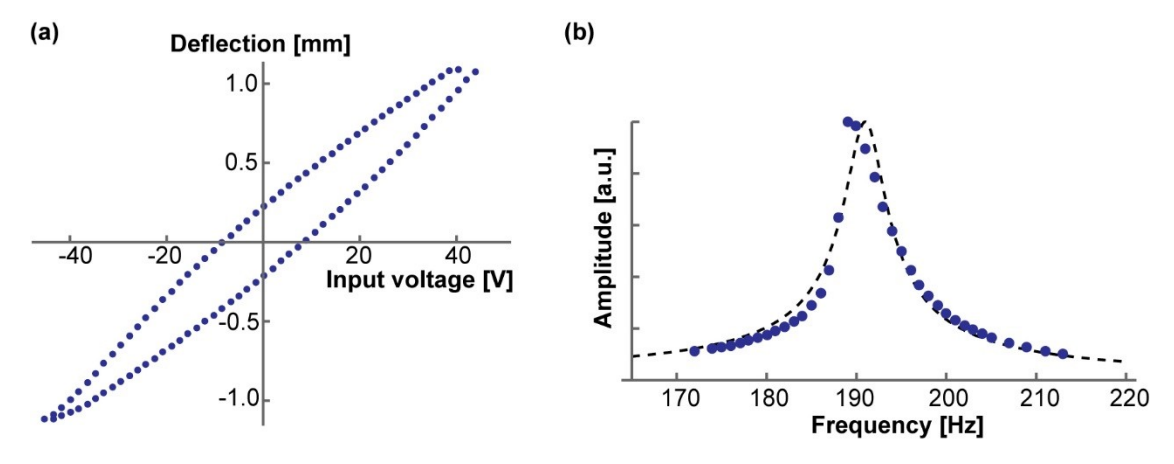


Figure 2. Characteristics of the piezoelectric bimorph actuator. (a) The applied voltage to the piezoplate versus the piezoplate deflection. Typical non-linear characteristic of piezoelectric material was quantified. (b) The frequency response of the piezo actuator given an initial input frequency and measuring the corresponding output amplitude. The dotted line is the curve fit to the theoretical frequency response of a damped harmonic oscillator. This graph allowed for the calculation of the resonant frequency (f_{pz}) , effective mass (m_{pz}) , Q factor (Q_{pz}) , and damping coefficient (c_{pz}) .

As with the 3D printed nylon cantilevers, the same method of analysis was employed to find the spring constant of the piezoplate. After incremental application force and optical analytics, the spring constant ($k_{\rm pz}$) was determined to be 565 N/m. The frequency response was measured by applying a sinusoidal voltage input to the piezoplate ranging in frequency from 1 Hz to 310 Hz. A small piece of aluminum foil was mounted onto the piezoplate and the change in mass ($\Delta m_{\rm pz}$) was measured.

The resonant frequency (f_{pz}) of the piezoplate was measured to be 189 Hz. With the resonant frequency and spring constant of the actuator, Equation (6) was used to find the effective mass of the piezoplate (m_{pz}).

$$f_{\rm pz} = \frac{1}{2\pi} \sqrt{\frac{k_{\rm pz}}{m_{\rm pz} + \Delta m_{\rm pz}}} \tag{6}$$

The Q factor (Q_{pz}) of the frequency response can then be calculated generally by locating the position where the output voltage has dropped to $1/\sqrt{2}$ of the maximum output voltage. Through the above listed methods, the Q factor of the piezo plate was calculated to be 47. Finally, using Equation (7) the damping coefficient (i.e. the viscous damping coefficient) was found to be 0.010.

$$c_{\rm pz} = \frac{\sqrt{(m_{\rm pz} + \Delta m_{\rm pz}) \cdot k_{\rm pz}}}{Q_{\rm pz}} \tag{7}$$

2.3 Design of the actuation Mechanism

Figure 3 shows the principle of the displacement transmission mechanism we developed for the tweezers. The moving arm of the tweezers is supported by a flexure and moved by a piezo bimorph actuator. A cam is designed to linearly transfer the deflection (d) of the actuator to the angular displacement (θ) of the flexure. As shown in Figures 3(a) and (b), the curve of the cam is given as the path, which the tangent point P traces as d and θ increase. In this theoretical model, the contact point moves by pure rolling without sliding, minimizing the friction between the cam and the actuator. For each combination of d and θ , the cam-piezo contacting point, P, is given as the closest point on the piezo to the point O, which is a fixed point within the cam (Figure 3(b)). The vector \overrightarrow{OP} is given as a function of d and θ :

$$\overrightarrow{\mathsf{OP}} = \mathbf{r}(\theta, d) \tag{8}$$

The plot of Equation (8) provides the trace of the contact point, which equals the curve of the cam. Here we assume the piezo-bimorph actuator to be a simple bi-layer cantilever, where one-layer contracts and the other expands resulting in a bending motion on application of a voltage (Figure 3(c)). With this assumption, the bending of the piezo actuator is expressed as:

$$y = d \left(\frac{x}{L}\right)^2 \tag{9}$$

Because of the hysteresis, application of the same voltage does not result in the same deflection of the piezo actuator as shown Figure 2(a). It is practical to linearly-correlate the angular displacement with the piezo mechanical deflection rather than the piezo control voltage. It is desired that the flexure bending angle θ should be linearly correlated with the piezo deflection d, to be expressed as follows:

$$\theta = k \cdot d \tag{10}$$

When Equation (10) is assumed, $\overrightarrow{OP} = \mathbf{r}(\theta, d)$ is given as a function of θ with k as a constant. The value of k should be so chosen such that magnitude of \mathbf{r} , i.e. the length of OP, is a monotonically decreasing function of θ . We used a custom MathematicaTM program to find the position of P and find $\mathbf{r} = \overrightarrow{OP}$ as a function of θ . Once the curve $\mathbf{r}(\theta)$ was found, curve fitting was used to find a circle closest to the curve. As shown in Figure 3(d), the center O' of the fitted circle is usually different from O which is used to find the curve. Calculated motion of this design is shown in the supplementary video 1. Note that it is also possible to design a cam that converts the piezo deflection to a linear displacement measured in the y-axis, or in the tip-to-tip direction. However, linear displacement is highly dependent on the tip design and how the pair of tips are arranged, and a cam needs to be designed for each specific experimental configuration. We chose the angular displacement as a design parameter because it is easily applicable to general, multiple experimental conditions.

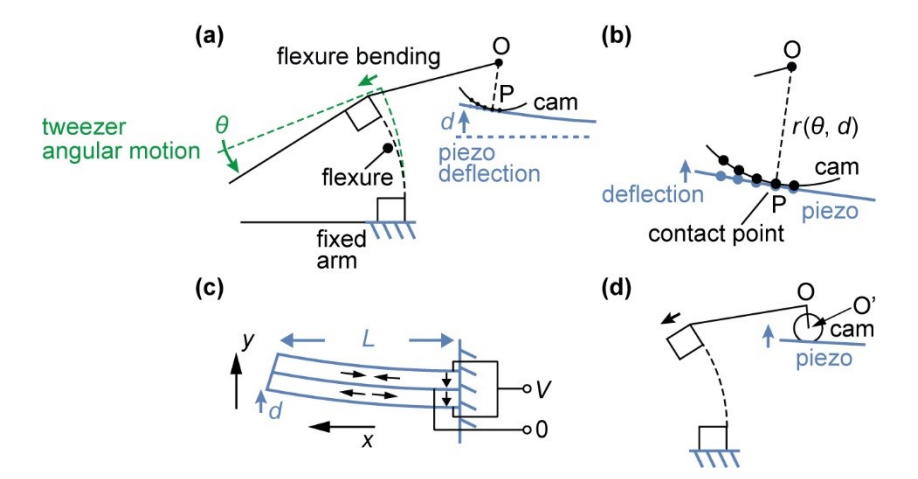


Figure 3. Principle of the displacement transmission mechanism. The cam is designed for θ to be linearly correlated to d. (a) The moving arm of the tweezers is supported by a flexure, and actuated by a piezo bimorph actuator. (b) The curve of the cam is given as a path traced by the point of contact. (c) Piezo bimorph actuator works in a similar way to a bimetal cantilever (d) The cam is approximated as a circle in the actual 3D design (see supplementary video 1).

2.4 System design

Figure 4 shows a photograph of the completely constructed system, which includes the flexure, piezoelectric bimorph actuator, and the working tweezer tips. The width and the length of the flexure are 4 mm and 10 mm, respectively. The designed thickness of the flexure's thinnest part is 0.8 mm. Additionally, the lower right corner shows a photograph of the microtweezer with tips fully open (corresponding to a -45 V supply to the piezoelectric bimorph actuator). In Figure 5, it can be seen that a simplified system block diagram consists of a linear model spring-dashpot system, also commonly referred to as the damped harmonic oscillator [19-20]. In this model, the associated spring constant of the system ($k_{\rm sys}$) is approximated as the summation of the spring constant of the tweezer flexure ($k_{\rm fl}$) and the spring constant of the piezo actuator ($k_{\rm pz}$). The other portion of the damped harmonic oscillator model is a viscous dashpot. Similarly, to that of the spring constant, the associated damping coefficient of our system ($c_{\rm sys}$) is the summation of the damping coefficient of the tweezer flexure ($c_{\rm fl}$) and the damping coefficient of the piezo actuator ($c_{\rm pz}$). Just the same is the representation of the piezo-tweezer system effective mass ($m_{\rm sys}$) is the summation of the effective mass of the tweezer-flexure ($m_{\rm fl}$) and the effective mass of the piezo actuator ($m_{\rm fl}$).

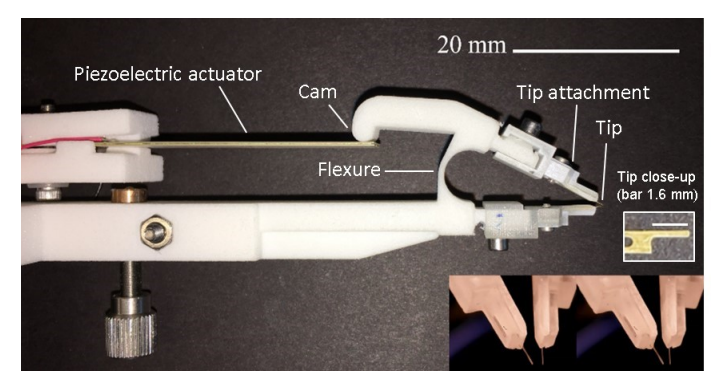


Figure 4. Photograph of the tweezer system.

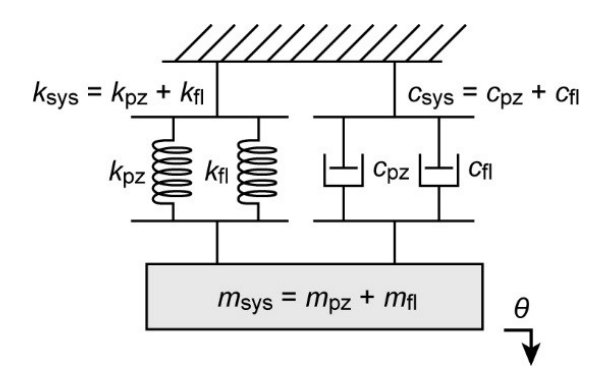


Figure 5. System block diagram.

Tweezer tips (L = $1600~\mu m$, W = $150~\mu m$, and t = $25~\mu m$) were patterned from a $25~\mu m$ -thick brass film (C260 brass, McMaster-Carr, IL) through standard lithography. The brass film was first sandwiched between two photoresist films (Micromark, NJ), the topside of which was patterned through UV exposure and development. The tweezer tips were then etched out with a ferric chloride solution (Micromark, NJ). A similar processs is reported in [21] for the fabrication of AFM cantilever. The attachment for the tips were 3D printed from UV curable acrylic polymer (Shapeways, NY) to hold the tips at the end of the arms. Tweezer tips can be easily replaced for each experiment . A close-up photograph of the brass tip is shown in a panel in Figure 4. The measured average spring constant of 6 probes was $1.3 \pm 0.1~N/m$.

3. Results

3.1 Comparison of computational and experimental models

We performed an FEM analysis to show that the experimentally discovered parameters can be adequately used to find the spring constant ($k_{\rm fl}$) and the resonant frequency ($f_{\rm fl}$) of arbitrary designed 3D printed part. The material properties used are those of the 3D printed nylon (PA2200) we showed in the previous section (Young's Modulus of 1700 MPa and the average density of 0.84 g/cm³). The designed width of the tweezer flexure was 0.8 mm. As previously explained, the size of this dimension was reduced during computation by 0.23 mm to more accurately represent the bulk characteristics of the material for COMSOL® analysis (see Figure 6(a)). The COMSOL® analysis yielded a spring constant equal $k_{\rm fl_COMSOL}$ = 240 N/m. The resonant frequency from the COMSOL® analysis was $f_{\rm fl_COMSOL}$ = 111 Hz.

Using the same force testing set up as the 18 cantilevers, the spring constant of the tweezer flexure was experimentally found to be $k_{\rm fl_measured}$ = 215 N/m with an applied force range of 0 N to 2.9 N (see Figure 6(b)). The difference between the experimental value and the COMSOL® simulated value is 25 N/m (percentage difference ~11%). Using a laser, an adhered piece of reflective aluminum, and a photodiode position detector, the resonant frequency of the tweezer flexure was experimentally determined. The resonant frequency of the tweezer flexure was found to be $f_{\rm fl_measured}$ = 121 Hz. These two frequencies have a difference of 10 Hz (percentage difference ~9%). The measured Q factor was ($Q_{\rm fl}$ = 170). The resonant frequency, the spring constant, the effective mass and the damping coefficient follows the same relationship as we described for the piezoactuator:

$$f_{\rm fl} = \frac{1}{2\pi} \sqrt{\frac{k_{\rm fl}}{m_{\rm fl} + \Delta m_{\rm fl}}} \tag{11}$$

$$c_{\rm cl} = \frac{\sqrt{(m_{\rm fl} + \Delta m_{\rm fl}) \cdot k_{\rm fl}}}{O_{\rm fl}} \tag{12}$$

Using equations (11) and (12), we found the tweezer flexure's effective mass ($m_{\rm fl}$ = 0.37 g), and the damping coefficient ($c_{\rm fl}$ = 0.0035).

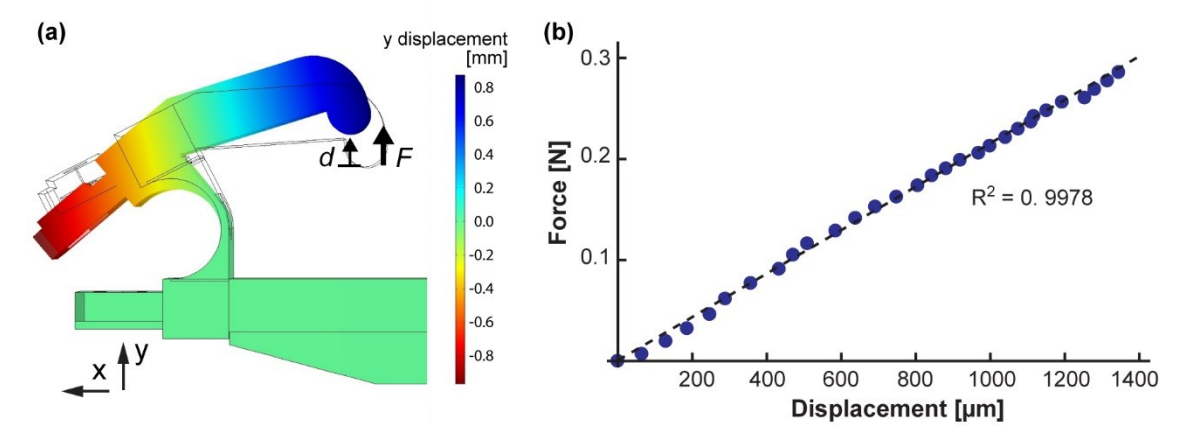


Figure 6. Once fundamental material properties are found, characteristics of an arbitrary designed part can be found from an FEM analysis. (a) COMSOL® analysis of the tweezer flexure. The image displays the cam with an applied force of 0.2 N. (b) Experimentally measured tweezer flexure force vs. displacement curve.

3.2 System performance

The 3D printed tweezer flexure, and the piezo actuator, the total system was characterized to determine the system frequency response. The frequency response was measured by applying a sinusoidal voltage input to the piezoplate ranging in frequency from 1 Hz to 310 Hz. A small piece of aluminum foil was mounted onto the outer surface of the tweezer's cam. As previously described, a laser was applied to the aluminum mount which reflects onto a photo-detector. We conducted this experiment for the system frequency response including and excluding the detachable tweezer tips (these tips vary based on project application). The results of this experiment are depicted in Figure 7. Because the spring constant of the working tip (1.3 N/m) is less than 1% of that of the flexure (215 N/m), the resonant frequency should not show measurable changes even when the working tips are touching an object. However, when the tip is immersed in water, we observed a slight effect of damping and the peak oscillating amplitude was reduced to ~90%, which corresponds to a ~10% increase in the system damping coefficient.

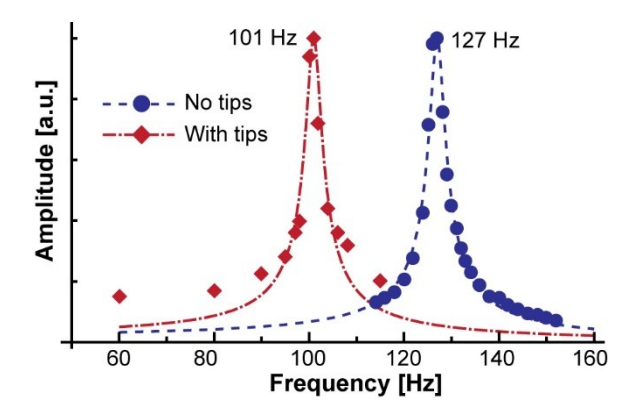


Figure 7. Frequency response of the system. The series in blue shows the frequency response of the piezo-tweezer system. The orange series is for the system with the attached tips. The resonant frequencies of 101 Hz and 127 Hz, with and without tips, respectively, are indicated.

In addition to the frequency characterization, we demonstrate that the actuation mechanism of the cam and the flexure linearly transfer the piezo deflection to the angular displacement of the tweezer tips wihin the full operational range of the actuator. The result is shown in Figure 8. The root-mean-square error from the linear fit was 0.1 degrees.

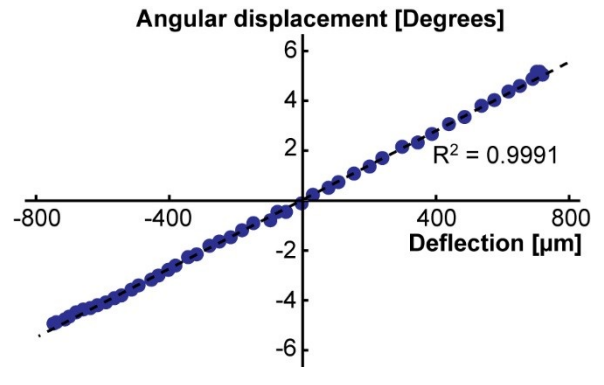


Figure 8. The above graph displays the angular displacement (degrees) of the tweezer tips plotted against the corresponding piezoplate displacement (m).

If we consider the simplified model as illustrated in Figure 5, the spring constant, the effective mass, and the damping coefficient of the system can be approximated as the summations of those of the tweezer flexure and the piezo actuator. When we use the values obtained in the previous sections, we find:

$$k_{\text{sys}} = k_{\text{fl}} + k_{\text{pz}} = 215 + 565 = 780 \text{ N/m}$$
 (13)

$$m_{\text{sys}} = m_{\text{fl}} + m_{\text{pz}} = 0.37 + 0.40 = 0.77 \text{ g}$$
 (14)

$$c_{\text{sys}} = c_{\text{fl}} + c_{\text{pz}} = 0.0035 + 0.010 = 0.014 \text{ Ns/m}$$
 (15)

When we use these values, the expected resonant frequency (f_{sys}) is calculated as:

$$f_{\rm sys} = \frac{1}{2\pi} \sqrt{\frac{k_{\rm sys}}{m_{\rm sys}}} = 160 \text{ Hz}$$
 (16)

which is comparable to the measured value of $f_{\rm sys} = 127\,$ Hz. When we use (13),(14) and the measured Q factor for the system without tips ($Q_{\rm sys} = 38$),

$$c_{\rm sys} = \frac{\sqrt{m_{\rm sys} \cdot k_{\rm sys}}}{Q_{\rm sys}} = 0.020 \text{ Ns/m}$$
 (17)

which is also comparable to the expected value shown in Equation (15).

4. Conclusion

We showed the design of an actuation mechanism based on a 3D printed flexure and a piezo bimorph actuator. The elastic modulus and the density of the 3D printed nylon were first determined by studying sets of simple cantilevers. The finite element method (FEM) analysis of the tweezers on COMSOLTM based on the obtained fundamental data matched well with the measurement. The angular displacement of the moving arm showed a good linearity ($R^2 = 0.9991$) with the linearity error

- of 0.1degrees within the actuator deflection (0-1.74 mm), showing the efficacy of the 3D printed cam.
- We have already utilized this manipulation systems in many successful applications we have
- 315 reported elsewhere [22-24]. In these previous studies, we used the tweezers for relative positioning
- 316 with incremental tip displacement. The smallest positioning step was defined by the resolution of the
- 317 voltage step sent from the controller, and the typical minimum operational step was ~1.7 μm/step at
- a voltage application of 0.35 V/step. In this paper, we described the detailed design principle and the
- 319 material and dynamic characteristics of the manipulation system. Our microtweezer design is a low-
- 320 cost efficient method of the direct assembly method of micro/meso-scale biosamples.
- 321 Supplementary Materials: The following are available online at www.mdpi.com/xxx/s1
- **Author Contributions:** conceptualization, K.H. and D.J.; methodology, K.H.; validation, A.A., G.A. and D.J.;
- formal analysis, A.A. and K.H.; investigation, K.H.; resources, K.H.; writing—original draft preparation, A.A.;
- writing—review and editing, G.A. and K.H.; supervision, project administration, and funding acquisition, K.H.
- Funding: This research was funded by the National Science Foundation (IDBR1555986 and CCSS1809047).
- 326 Conflicts of Interest: The authors declare no conflict of interest. The funders had no role in the design of the
- 327 study; in the collection, analyses, or interpretation of data; in the writing of the manuscript, or in the decision to
- 328 publish the results.

329 References

- M. Sitti and H. Hashimoto, "Controlled pushing of nanoparticles: modeling and experiments," *IEEE/ASME Transactions on Mechatronics*, vol. 5, (2), pp. 199-211, June, 2000.
- J. Hou et al, "AFM-based robotic nano-hand for stable manipulation at nanoscale." *IEEE Transactions on Automation Science and Engineering* 10 (2), pp. 285-295, 2012
- 334 3. H. Chen and D. Sun, "Moving groups of microparticles into array with a robot–tweezers manipulation system." *IEEE Transactions on Robotics* 28(5), pp. 1069-1080, 2012.
- K. Kim et al, "Nanonewton force-controlled manipulation of biological cells using a monolithic MEMS microgripper with two-axis force feedback," *J Micromech Microengineering*, vol. 18, (5), pp. 055013, April, 2008.
- 5. N. Chronis and L. P. Lee, "Electrothermally activated SU-8 microgripper for single cell manipulation in solution," *J Microelectromech Syst*, vol. 14, (4), pp. 857-863, August, 2005.
- M. Boudaoud and S. Regnier, "An overview on gripping force measurement at the micro and nano-scales using two-fingered microrobotic systems." *International Journal of Advanced Robotic Systems* 11(3), p. 45, 2014.
- L. Tanner, "FDA takes fresh look at robotic surgery," USA Today, 09-Apr-2013. [Online]. Available:
 https://www.usatoday.com/story/news/nation/2013/04/09/robot-surgery-fda/2067629. [Accessed: 26-Feb-2018].
- 8. S. Kang *et al*, "Robotic thyroid surgery using a gasless, transaxillary approach and the da Vinci S system: the operative outcomes of 338 consecutive patients," *Surgery*, vol. 146, (6), pp. 1048-1055, December, 2009.
- Y. Kakeji et al, "Robotic laparoscopic distal gastrectomy: a comparison of the da Vinci and Zeus systems,"
 The International Journal of Medical Robotics and Computer Assisted Surgery, vol. 2, (4), pp. 299-304, September,
 2006.
- 351 10. D. B. Camarillo, T. M. Krummel and J. K. Salisbury, "Robotic technology in surgery: past, present, and future," *The American Journal of Surgery*, vol. 188, (4), pp. 2-15, October, 2004.
- 353 11. A. A. Ramadan *et al*, "Developmental process of a chopstick-like hybrid-structure two-fingered 354 micromanipulator hand for 3-D manipulation of microscopic objects," *IEEE Trans. Ind. Electron.*, vol. 56, (4), pp. 1121-1135, March, 2009.
- 356 12. A. Shelyakov *et al*, "Melt-spun thin ribbons of shape memory TiNiCu alloy for micromechanical applications," *International Journal of Smart and Nano Materials*, vol. 2, (2), pp. 68-77, March, 2011.
- R. Velazquez et al, "A low-cost highly-portable tactile display based on shape memory alloy micro-actuators," in Virtual Environments, Human-Computer Interfaces and Measurement Systems, 2005.
 VECIMS 2005. Proceedings of the 2005 IEEE International Conference On, July, 2005.
- 361 14. A. Alogla *et al*, "Micro-tweezers: Design, fabrication, simulation and testing of a pneumatically actuated
 362 micro-gripper for micromanipulation and microtactile sensing," *Sensors and Actuators A: Physical*, vol. 236,
 363 pp. 394-404, December, 2015.

- 364 15. H. S. Fiaz, C. R. Settle and K. Hoshino, "Metal additive manufacturing for microelectromechanical systems:
 365 Titanium alloy (Ti-6Al-4V)-based nanopositioning flexure fabricated by electron beam melting," *Sensors and Actuators A: Physical*, vol. 249, pp. 284-293, October, 2016.
- 367 16. Wei, Huaxian, et al. "Fabrication, Experiments, and Analysis of an LBM Additive-Manufactured Flexure
 368 Parallel Mechanism." *Micromachines* 9(11), 572, 2018.
- J. Parthasarathy, B. Starly, S. Raman, and A. Christensen, "Mechanical evaluation of porous titanium
 (Ti6Al4V) structures with electron beam melting (EBM), "Journal of the mechanical behavior of biomedical
 materials, 3(3), 249-259, 2010.
- 372 18. S. Zhao, S. J. Li, W. T. Hou, Y. L. Hao, R. Yang, and L. E. Murr, "Microstructure and mechanical properties
 373 of open cellular Ti–6Al–4V prototypes fabricated by electron beam melting for biomedical applications."
 374 Materials Technology 31(2) pp. 98-107, 2016.
- J. X. Zhang and K. Hoshino, Molecular Sensors and Nanodevices: Principles, Designs and Applications in
 Biomedical Engineering, December, 2013.
- P. Avitabile, "Numerical Evaluation of Displacement and Acceleration for A Mass, Spring, Dashpot
 System," In Proceedings of the 2004 American Society for Engineering Annual Conference & Exposition. 2004.
- 379 21. M. Michałowski and S. Łuczak, "AFM cantilevers with spherical tip of millimeter size." *Journal of Micromechanics and Microengineering* 29(1), 017002, 2018.
- 381 22. D. Jaiswal *et al*, "Stiffness analysis of 3D spheroids using microtweezers," *PLoS One*, vol. 12, (11), pp. e0188346, November, 2017.
- Devina Jaiswal, Zoe Moscato, Yuji Tomizawa, Kevin P. Claffey, and Kazunori Hoshino, "Elastography of multicellular spheroids using 3D light microscopy," *Biomedical Optics Express* 10(5), 2409-2418, 2019.
- Yuji Tomizawa, Krishna Dixit, David Daggett, and Kazunori Hoshino, "Biocompatible Cantilevers for
 Mechanical Characterization of Zebrafish Embryos using Image Analysis," Sensors 19(7), 1506, 2019.



© 2019 by the authors. Submitted for possible open access publication under the terms and conditions of the Creative Commons Attribution (CC BY) license (http://creativecommons.org/licenses/by/4.0/).